A Novel Approach to Contamination Suppression in Transmission Detectors for Radiotherapy

L. Beck, J. J. Velthuis, R. F. Page, R. P. Hugtenburg, C. De Sio, and J. Pritchard

***Abstract*—The current trend in X-ray radiotherapy is to treat cancers that are in difficult locations in the body using beams with a complex intensity profile. Intensity-modulated radiotherapy (IMRT) is a treatment which improves the dose distribution to the tumor whilst reducing the dose to healthy tissue. Such treatments administer a larger dose per treatment fraction and hence require more complex methods to verify the accuracy of the treatment delivery. Measuring beam intensity fluctuations is difficult as the beam is heavily distorted after leaving the patient and transmission detectors will attenuate the beam and change the energy spectrum of the beam. Monolithic active pixel sensors (MAPSs) are ideal solid-state detectors to measure the 2-D beam profile of a radiotherapy beam upstream of the patient. MAPS sensors can be made very thin (∼30 μm) with still very good signal-to-noise performance. This means that the beam would pass through the sensor virtually undisturbed (<1% attenuation). Pixel pitches of between 2 μm to 100 μm are commercially available. Large area devices (∼15 x 15 cm^2) have been produced. MAPS can be made radiation hard enough to be fully functional after a large number of fractions. All this makes MAPS a very realistic transmission detector candidate for beam monitoring upstream of the patient. A remaining challenge for thin, upstream sensors is that the detectors are sensitive to the signal of both therapeutic photons and electron contamination. Here, a method is presented to distinguish between the signal due to electrons and photons and thus provide real-time dosimetric information in very thin sensors that does not require Monte Carlo simulation of each linear accelerator treatment head.**

***Index Terms*—Clinical/preclinical evaluation/application studies, dosimetry for radiation-based medical applications, monolithic active pixel sensors (MAPSs), Monte Carlo simulations for imaging and therapy, radiation detectors for medical applications, radiotherapy verification.**

Manuscript received December 6, 2019; revised February 21, 2020; accepted April 2, 2020. Date of publication May 15, 2020; date of current version September 2, 2020. This work was supported by the Science and Technology Facilities Council under Grant ST/S000143/1. *(Corresponding author: L. Beck.)*

L. Beck, R. F. Page, C. De Sio, and J. Pritchard are with the School of Physics, University of Bristol, Bristol BS8 1TL, U.K. (e-mail: lana.beck@bristol.ac.uk).

J. J. Velthuis is with the School of Physics, University of Bristol, Bristol BS8 1TL, U.K., also with Swansea University Medical School, Swansea SA2 8PP, U.K., and also with the School of Nuclear Science and Technology, University of South China, Hengyang 421001, China.

R. P. Hugtenburg is with Swansea University Medical School, Swansea SA2 8PP, U.K., also with the Department of Medical Physics and Clinical Engineering, Abertawe Bro Morgannwg University Hospital Board, Swansea SA2 4QA, U.K., and also with the School of Physics, University of Bristol, Bristol BS8 1TL, U.K.

Color versions of one or more of the figures in this article are available online at http://ieeexplore.ieee.org.

Digital Object Identifier 10.1109/TRPMS.2020.2995059

I. Introduction

RADIOTHERAPY is one of the most prevalent treatments for cancer, where 40% of cured cancers used radiotherapy treatments in the U.K. [1]. It has been shown that delivering shorter, more intense treatments with megavoltage photon beams, improves the chances of treatment success [2]. Hence, this treatment strategy has seen increasing use in recent years, with the added advantages of reducing the number of times each patient must visit, and reducing National Health Service (NHS) waiting times for radiotherapy treatments. The use of higher dose rates has been made possible through the increased treatment precision afforded by intensity-modulated radiotherapy (IMRT) and volumetric modulated arc therapy (VMAT). These modalities treat cancers that are in difficult locations in the body using megavoltage photon beams with a complex intensity profile. IMRT treatments deliver the radiation from multiple angles with static or dynamic fields shaped by (up to 160) leaves of the multileaf collimator (MLC). In VMAT treatments the MLC leaves are dynamically moved while the gantry rotates around the patient. The higher intensity of these treatments means they pose a greater risk to the patient should the machine deviate from the treatment plan. With many moving mechanical parts, tracking them to ensure they are in the right position is an additional safety measure, external to the linear accelerator's (linac) own systems, to verify that the treatment is being performed correctly. This real-time treatment monitoring is known as *in-vivo* dosimetry. *In-vivo* dosimetry can be performed before or after the beam has passed through the patient. Measuring the beam after it has passed through the patient has the advantage of showing the patient alignment with the treatment beam. However, measuring beam intensity fluctuations downstream of the patient is difficult as the beam is heavily distorted. Transmission detectors are positioned upstream of the patient, sampling the beam before it is scattered in the patient's body. Hence, they can measure MLC positions with a higher precision. The signal response is composed of the therapeutic photons and electrons generated predominantly by Compton scattering in the flattening filter and collimators in the linac head, as well as in the air. For a 6-MV linac the photon spectrum peaks at around 2 MeV with ∼ 60% of photons having energies between 1 and 3 MeV. The electron contamination spectrum contains ∼ 20% of electrons with energy between 0.1 and 0.5 MeV and ∼ 75% with <2 MeV. In order to extract dose information, transmission detectors conventionally use a thick converter layer to generate signal from Compton scattering of the photon

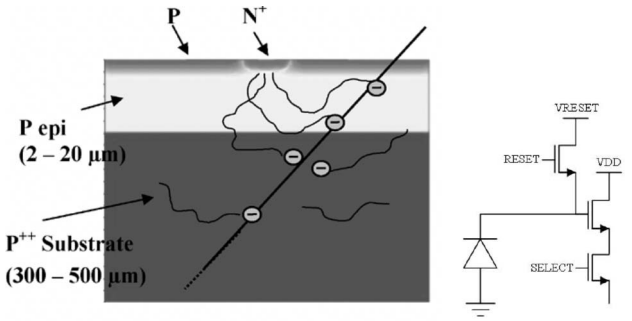

Fig. 1. Schematic cross section of a MAPS (left) and the in-pixel circuitry of a standard 3T MAPS device (right). The P++ substrate layer can be thinned to < 10 μm.

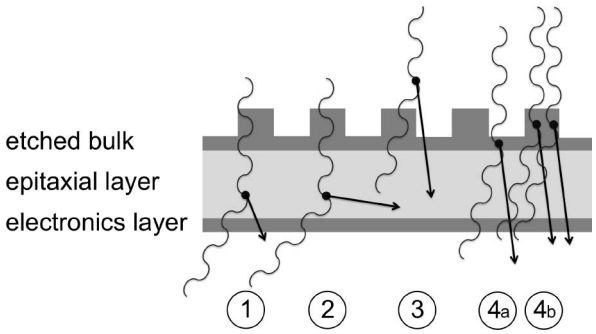

Fig. 2. Compton scattering of a photon in the epitaxial layer (1, 2), in the air/linac (3), and in the grating etched in the bulk (4).

beam. The large signal generated from the photons renders any signal contamination from electrons generated in the head of linac/in the air, negligible by comparison. Hence, the dose to the patient can be derived from the measured photon signal in these devices by using a treatment planning system [3]–[7].

However, these detectors attenuate the beam and change its energy spectrum. Modeling a transmission device in the treatment planning system is complex whilst modeling with Monte Carlo is difficult, with long computing times [8]. The current devices on the market, *ScandiDos Delta4 discover* [9], a solid-state detector, and the *Dolphin* [10], an ionization chamber system, have beam attenuations of $1.71\% \pm 0.02\%$ and $\sim$ 10% at 6 MV, respectively. The *DAVID* sensor is a flat plate ionization chamber which has signal readout wires positioned under each MLC leaf edge. The device specification is, therefore, customized for different types of MLC. The build-up material required to create a sufficiently measurable signal for MLC edge detection produces a beam attenuation of $4.7\% \pm 0.001\%$ [11] at 6 MV. The IQM is a large area position-sensitive ion chamber device, which has an attenuation of $5.43\% \pm 0.02\%$ at 6 MV [12]. In this article, a new approach to dosimetry is presented, in which no additional conversion layer is used, resulting in a beam attenuation below 1% [13], which is required by clinicians for real-time monitoring devices to be used in a clinical setting without additional calibrations in the treatment planning system.

A. Monolithic Active Pixel Sensor

We have been developing live treatment monitoring using a monolithic active pixel sensors (MAPSs) [14] system. Clinically, this device would be mounted on the linac treatment head. MAPS have the sensor matrix and pixel readout integrated into a single silicon wafer. These sensors are ideal as they can be made very thin while maintaining a good ratio of signal to noise and have negligible impact on the beam, attenuating the photon beam by less than 1% [13]. A schematic drawing of a three transistor (3T) MAPS sensor is shown in Fig. 1. When a charged particle traverses the sensor, electron—hole pairs are generated. The generated electrons are confined in the potential well between the lightly doped epitaxial layer and the highly doped substrate. No external bias voltage is applied. The electrons diffuse through the epitaxial layer until they reach the depleted zone underneath the diode. Here, the electrons are collected. The amount of collected electrons affects the gate voltage of the source follower and hence affects the current when the select switch is opened.

The top layer that houses the transistors is less than a micron thick. The epitaxial layer, the layer where signal generation takes place, is typically between $\sim$2 and $\sim$20-μm thick. The first couple of microns of the substrate layer are needed to create the built-in potential difference. The rest is only used for mechanical support.

Hence, the device can be made less than $\sim$30 μm thick, without loss of signal-to-noise, by thinning the device from the back. This means that the beam would pass through the sensor almost undisturbed ($<<1\%$ attenuation). Of course, an extremely thin sensor, used without any conversion material will be more significantly affected by the presence of the contamination electrons compared to the signal photons. Hence, in this article, a method is proposed to separate the electron and photons signals, allowing the photon fluence to be determined. This article has centered around the Achilles 3T MAPS sensor [15] which is $\sim 5 \times 5$ cm^2 with a total thickness of 100 μm. It has 4096×4096 square pixels with a pitch of 14 μm. Radiation damage studies have shown that the Achilles remained operational when tested with up to 300 million electrons per pixel [15]. This equates to approximately 20-K treatment fractions (at 2 Gy per fraction). Typically around 12-K treatment fractions are delivered per year in a radiotherapy suite. We have previously shown with the Achilles sensor mounted on the linac head, that we can achieve a leaf edge resolution of 52 ± 4 μm at the isocenter for leaves with a width of 1 cm using 0.1 s of data taken at 400 MU/min for static fields [16]. We have also shown that it is possible to monitor dynamic treatments with continuously moving leaves [13].

II. Method : Patterning the Sensor

For dosimetry it is essential to only measure the signal due to incoming photons as they will deposit the dose in the tumor. A method was developed to separate the photon and electron signal by exploiting the Compton scattering in the nonsensitive bulk layer of the MAPS. With the beam incident on the backside of the sensor, it will traverse the bulk before the epitaxial layer (back-illuminating). The number of electrons produced by Compton scattering of the photons can be modulated by changing the thickness of the bulk layer [see (4a) and (4b)

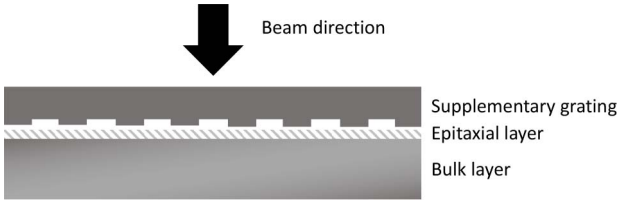

Fig. 3. Schematic of the grating placed face down on the front-side of the Achilles.

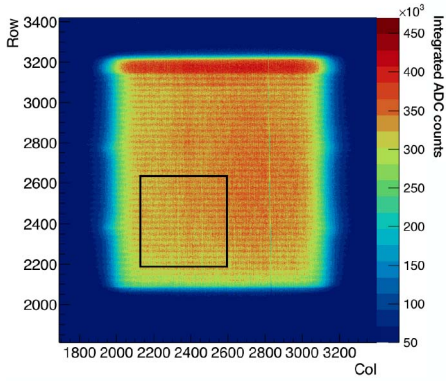

Fig. 4. Response from the MAPS sensor where the presence of the photon field upon the strips is evident. The region of interest used for further study is indicated. There is some signal saturation in defective rows of the sensor in this prototype device.

in Fig. 2] [17]. The simplest approach is to etch strips into the bulk layer of the MAPS. This does not alter the number of Compton electrons generated by photons in the epitaxial layer (1 and 2) or air (3). However, it does lead to an increase of Compton electrons in the strips compared to the thin area; comparing (4b) with (4a). For a sufficiently thin bulk layer, the signal from contamination electrons (3) will have a negligible difference between peaks and troughs of the grating. Hence, the photon contribution can be deduced by comparing the signal from under a strip or under a trench.

III. Experimental

As a proof-of-principle study, a piece of 300-μm thick silicon, etched with 50-μm deep trenches, was placed on top of the MAPS as an alternative to etching the sensor directly. The grating pattern formed from the etching was placed face down on the sensor, as shown in Fig. 3. This was to minimize the amount of scattering through extra material if the grating were placed face up, which would make the pattern more diffuse before reaching the epitaxial layer. A number of square field sizes were delivered using an ElektaTM AgilityTM linac: 3×3 cm^2, 4×4 cm^2, 5×5 cm^2, 6×6 cm^2, and 7×7 cm^2 at the isocenter. Fields are shaped using the MLC and Y-jaws. Fig. 4 shows the enhanced signal where the 3×3 cm^2 6-MV photon beam is incident upon the MAPS sensor, which was placed at the isocenter.

The 2-D sensor output is projected in 1-D along the grating, across 400 columns, clearly showing the modulation of the photon contribution as shown in Fig. 5. It was first checked that the pitch of the gratings obtained from the analysis was

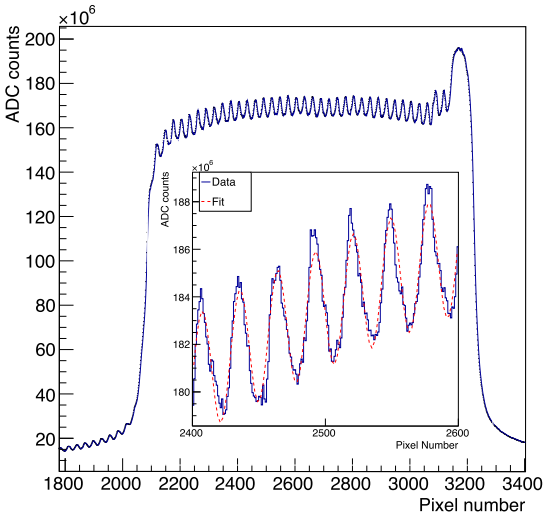

Fig. 5. Profile of signal response perpendicular to the gratings. Inset: Fitted data for a 7×7 cm^2 field.

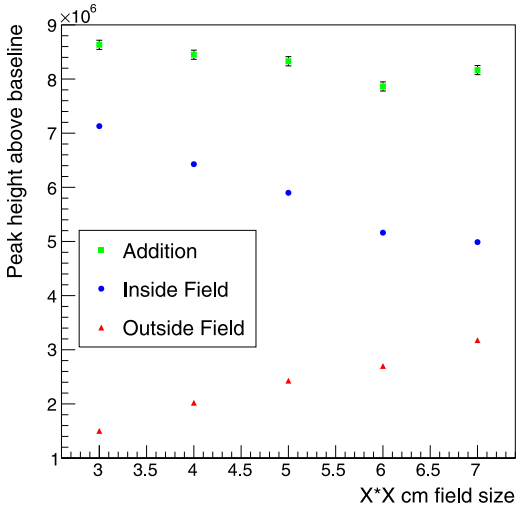

Fig. 6. Signal peak height extracted from the amplitude of the fitted sinusoidal wave inside the photon field, outside the photon field and the addition of the two.

consistent with the pitch known to be etched into the silicon. A fit was made in the region of interest (shown on Fig. 4) of the sensor where the photon field is present. A second-order polynomial was fitted, to account for the background shape of the field. A sinusoidal wave was used as a simple approximation for small strip pitches to fit the periodic pattern caused by the grating. The grating pitch was found to be 398.8 ± 0.2 μm for all the field sizes, whilst the true pitch is known to be 400 ± 10 μm. An example of the fit overlaid on the data is shown in Fig. 5 (inset).

The additional photon contribution due to the grating should be proportional to the amplitude of the fitted sinusoidal wave and independent of field size. Fig. 6 shows the peak height over the background baseline shape for a range of field sizes. Projections along the grating were taken across 400 columns inside the field and 400 columns outside the field. A sensor area was defined outside the field at least 1 cm from the photon field edge. It can be seen that within the photon field the peak height decreases with increasing field size. This is

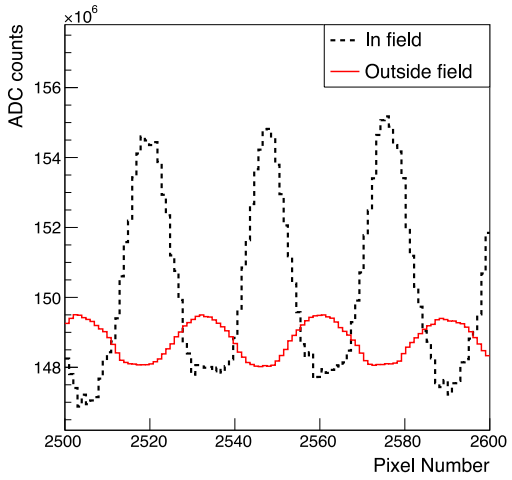

Fig. 7. Signal modulation predominantly from photons inside the photon field. Outside the field modulation is mainly due to electron scattering in the strips.

because the contamination electron background increases with field size [18], with an anti-phase signal response primarily due to scattering out of the sides of the peaks into the epitaxial layer below the troughs of the grating. The stopping of low energy electrons does not have a significant impact on the signal response as higher energy electrons lose energy through the grating and compensate for this. Fig. 7 shows the signal response inside the photon field and outside the photon field along the same strips. Outside the photon field only the diffuse contamination electron background contributes. It can be seen that the signals are out of phase and thus the apparent amplitude is lower. The peak height over baseline outside of the field is also shown as a function of field size in Fig. 6 and as expected the amplitude of the electron signal is also proportional to the field size, reflecting the increase in the electron background. The electron background was measured at the same point on the detector, outside of all the measured fields. Therefore, it will not exactly represent the electron contamination at the point measured inside the photon field as the intensity of the electron contamination varies across its field. It is only shown as a proof-of-principle concept. Hence, the sum of the two contributions is approximately flat across different field sizes, denoted as "addition" in Fig. 6. This shows that the peak height signal due to the photons themselves is constant as a function of the field size and that if the electron contamination signal is removed, the signal modulation will be representative of the photon fluence. The difference between the peak and trough regions was 50 μm. To mitigate against the modulation of the signal from electron contamination, the grating can be made a combination of thinner and wider such that, regions under the middle of peaks and troughs can be identified where the scattering of electrons out of the sides of the peaks does not have an impact. Note by changing the grating geometry such that the electron contamination background has a constant flat signal response means there is no need to measure the electron contamination outside of the field. Thus, the signal will only significantly modulate due to the increased Compton scattering under the peaks and the photon fluence can be extracted.

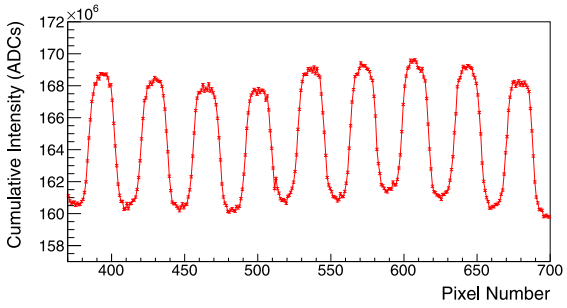

Fig. 8. Profiles taken for a 5×5 cm^2 field, integrated across 400 columns of the sensor with the linac beam incident upon a 2-mm pitch grating structure.

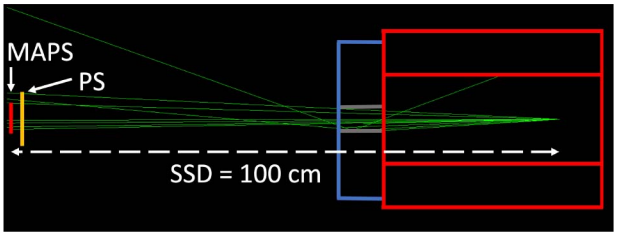

Fig. 9. Linac was modeled simply as a Tungsten box with an opening that projects to specified field sizes at isocenter. The position of the MAPS detector and the phase space plane used, are indicated.

IV. Alternative Grating Size

A 2-mm pitch grating was also tested and a profile taken across 400 columns is shown in Fig. 8 for a 5×5 cm^2 field size. It can be seen that the wider pitch means that the signal can plateau in the peaks and troughs and may be preferable for subtracting a constant electron background in the plateaued regions. Out of field measurements were not possible in this experiment as this grating structure was larger than the field sizes tested. This will be the work of future studies. The optimal grating pitch determines the granularity of dosimetry and will depend on the angular spread of the scattered electrons due to the difference in thickness between the peaks and troughs.

V. Simulation

To confirm the experimental results, a simulation study was performed using Gate [19], which is a software package based on Geant4 [20], developed for use in studies of medical imaging and radiotherapy. Simulations for generating the electron contamination were particularly computationally intensive and required 10^{13} initial photons to be simulated for the 3×3 cm^2 field and the number of photons was proportionally scaled for larger field sizes to maintain the same number of photons per unit area. Hence, the simulations were distributed across ten 64-core AMD EPYC bare metal compute nodes using Oracle cloud infrastructure [21]. The compute nodes were created using an on-demand elastic cluster using the cluster in the cloud system [22]. The isotropic cone beam of photons with energies derived from the Mohan energy spectrum [23] was propagated from the point where the target would be positioned inside the linac treatment head, as shown in Fig. 9. The full linac head was not simulated as the purpose of this article

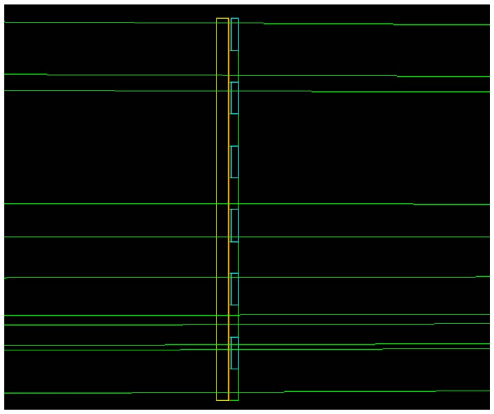

Fig. 10. Gratings of 300-μm thickness and trench depth of 50-μm face down on the epitaxial layer of the sensor. The beam is coming from right to left.

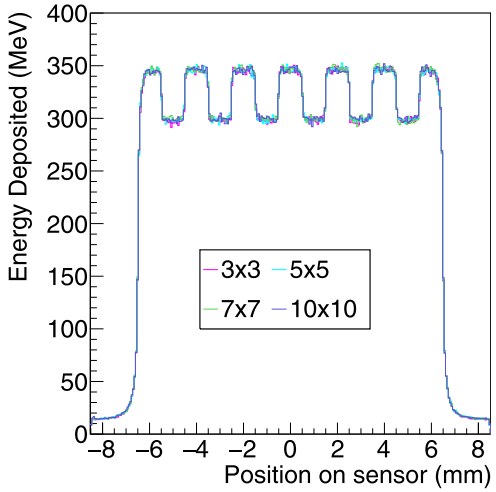

Fig. 11. Simulation output of the energy deposited in the epitaxial layers for photons only, after passing through the grating.

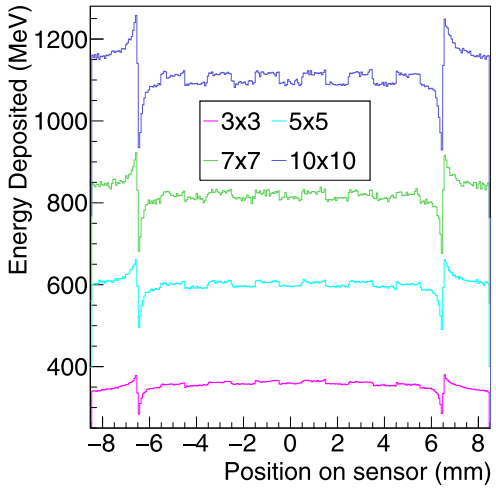

Fig. 12. Simulation output of the energy deposited in the epitaxial layers for electrons only, after passing through the grating.

was to show that any beam consisting of electrons and photons can be separated into its individual particle type components, rather than needing to simulate the specific beam from a particular treatment head. Jaw collimators were simulated as 8-cm thick blocks of Tungsten to shape the beam into field sizes of 3×3 cm^2, 5×5 cm^2, 7×7 cm^2, and 10×10 cm^2 as projected at the isocenter. The electron contamination from the collimators and ionization chamber were omitted as this contribution is highly diffuse and occupies only 0.1% of the solid angle at isocenter, where the measurements were taken and the sensor was simulated at a source-surface distance (SSD) of 100 cm. The simulated silicon strip structure has a 2-mm pitch, i.e., 1-mm trench width and 1-mm peak width as used for Fig. 8. The grating is 300-μm thick with a trench depth of 50 μm and is placed face down on the epitaxial layer of the sensor. Only a small area is simulated to save time, for the grating it is 13-mm wide, consisting of seven peaks and six trenches, and 10-mm long. It sits on top of a 17-mm wide and 12-mm long subset of the sensor, such that there is a periphery around the grating where the sensor is exposed to the beam with no grating present. The Achilles sensor is replicated with a 10-μm epitaxial layer and total thickness of 100 μm. Energy deposits are saved in 14×14 μm voxels to simulate the Achilles pixels. The Geant4 electromagnetic physics list *emstandard_opt3* was used for its higher accuracy in electron tracking [20] and Urbán model of multiple scattering [24]. A step limit of 3 μm was set for electrons, positrons, and photons passing through the grating and epitaxial layer of the sensor. Decreasing the step limit further had no impact on the results and increased compute time. Particles incident on the sides or back of the linac head were killed to save compute time. The beam was propagated through an air-filled world until just before the grating and sensor, where the photons and electrons were saved separately into phase space files.

The therapeutic photon and contamination electron contributions could then be separately propagated through the grating and sensor, as shown in Fig. 10. The phase space file was rotated by 90 degrees and recycled three more times.

The energy deposited in the epitaxial layer is shown in Fig. 11 for photons and Fig. 12 for electrons. The energy deposits are summed across 100 pixel columns for 10^{10} incident photons per cm^2.

In Fig. 11 it can quite clearly be seen that the photon signal is independent of field size and that the grating pattern is very evident. There is an enhancement of the signal where the seven peaks are located above the six trench areas.

In Fig. 12 it can be seen that the energy deposited by contamination electrons in the sensor increases with increasing field size. Furthermore it can be seen that the pattern is antiphase to that shown in Fig. 11, confirming the experimental findings in Fig. 7. It should be noted that in Figs. 11 and 12 the total energy deposited in the silicon is shown, as opposed to the analogue-to-digital converted (ADC) units read out from the sensor. Hence, charge sharing between pixels is not accounted for. It is apparent from the dips in signal at the edge of the supplementary piece of the patterned silicon at ±6.25 mm and subsequent increase in signal immediately outside of the grating, that the shape of the peaks is also influenced by a larger amount of electron scattering out of the thicker strips of the grating than in the thinner strips.

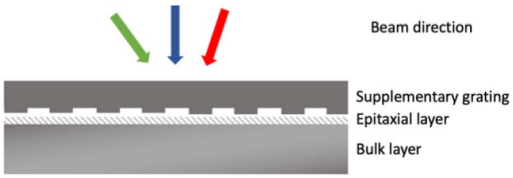

Fig. 13. Schematic of incident beam angles on the 4-mm pitch grating.

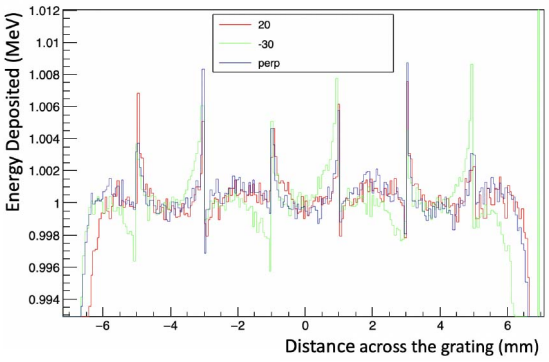

Fig. 14. Normalized simulated energy deposit in the epitaxial layer from an electron beam incident at 0, 20, and −30 degrees for a 4-mm pitch grating. There are three troughs, one of which is in the centred at 0, and 4 peaks.

A. Toward Deployable Grating Structure

The experimental results presented in this article show that the concept of a grating can indeed be used to extract the signal by photons after correcting the total signal for the signal deposited by electrons. For a deployable device, it is key that the electron signal is constant throughout the detector such that the signal is modulated by the photons only. This can be achieved by making the grating thin and wide enough. For a grating structure with a 4-mm pitch (2-mm trench and 2-mm peak width) with the same thickness as our experimental grating three simulations were produced with electrons incident on the grating at 0, 20, and −30 degrees, as indicated in Fig. 13. The electron energy spectrum was taken from the previously mentioned simulation. In Fig. 14 the simulated deposited energy by the electrons in the epitaxial layer across 100 pixel columns is shown. Each distribution has been normalized to the average signal under the middle ten pixels of the peaks and troughs so the scattering patterns can be seen with respect to the incoming electron angle. Besides the spikes at the grating edges, the signal due to electrons is essentially flat. Hence, it is apparent that the anti-phase pattern is due to the scattering from the thicker peak sections of the grating into the air gap under the troughs. This shows that for an appropriately designed grating structure, there is no need to measure the electron signal outside the field as the signal from the pixel region under the middle of the peaks and troughs can be used, avoiding the scattering at the sides. Hence, only the photon signal will be causing a modulation in the sensor response, and thus the photon fluence and subsequently the dose information, can be extracted directly. A study to determine the optimal dimensions of the grating is currently in progress.

VI. Discussion

In order to obtain the dose received by a patient, only signals generated by photons are required. Contamination electrons generated in the linac head and air also generate signal in MAPS sensors. Despite the lower flux of contamination electrons their contribution to the total signal is larger than that deposited by the photons due to the much larger interaction cross section of electrons with silicon. In this article, we have shown that the signals generated in MAPS from electron contamination and therapeutic photons are dependent on the thickness of material traversed before the epitaxial layer in the sensor. This can be achieved by patterning the bulk layer of the MAPS with strips and back-illuminating the sensor to the beam such that the beam will traverse the pattern before the epitaxial layer. If the bulk is made sufficiently thin [$\mathcal{O}(50\ \mu\text{m})$] then the electron signal will be relatively flat compared to the modulated photon signal, with the added advantage of having $<1\%$ beam attenuation, which clinicians require for real-time monitoring devices to be accepted into clinical use without additional calibrations. The signal modulation observed experimentally was confirmed in simulation using the Mohan energy spectrum for a 6-MV photon spectrum and the contamination electrons generated in the air and linac jaws from those photons. In future iterations of the simulation, the sensor will be modeled at the linac head. Then it will be necessary to include contamination electrons from the other components of the linac head, such as the flattening filter, where the angular and spatial distribution will differ from that at the isocenter. Further experiments will be performed on different topologies of the grating structure, including much thinner gratings. It has been shown that the electron contamination reduces with distance from the linac head [25], [26], hence in the future we will include studies at different SSDs. The trench dimensions and overall thickness of the grating will be optimized to minimize the contribution from contamination electrons to the modulation total signal, allowing the photon signal to be extracted. After this, we will determine a mapping between the 2-D photon signal generated in the sensor and a 3-D dose profile as has been shown for the Magic Plate [7] and Octavius 4D [27].

VII. Conclusion

It is necessary to develop new techniques to monitor the increasingly complex IMRT treatments being used for targeting cancerous tumors. MAPSs are highly appropriate devices for real-time upstream dose monitoring due to their $<1\%$ beam attenuation at 6 MV. They also have an excellent position resolution of $52 \pm 4\ \mu$m at the isocenter for leaves with a width of 1 cm using 0.1 s of data for static fields. Producing a pattern of strips into the nonactive bulk layer of the back-illuminated sensor has been shown to be a successful method of distinguishing the contributions of therapeutic photons and contamination electrons and the phenomenon has been confirmed in simulation. This will allow the dose to the patient to be accurately obtained in realtime without relying on Monte Carlo simulation of each individual linac treatment head.

ACKNOWLEDGMENT

The authors would like to thank Teledyne e2v for providing the silicon grating structures and to Oracle for providing access to high performance cloud infrastructure (compute and storage) to run simulations. They thank Alex Scorrer for fruitful discussions and to Phil Bates (Oracle) for advice on appropriate cloud infrastructure to run simulations. They also thank Chris Edsall and Christopher Woods for their advice on using the Cluster in the Cloud.

REFERENCES

[1] S. M. Bentzen *et al.*, "Towards evidence-based guidelines for radiotherapy infrastructure and staffing needs in europe: The ESTRO QUARTS project," *Radiotherapy Oncol.*, vol. 75, no. 3, pp. 355–365, 2005.

[2] L. C. Cho, R. Timmerman, and B. Kavanagh, "Hypofractionated external-beam radiotherapy for prostate cancer," *Prostate Cancer*, vol. 2013, Mar. 2013, Art. no. 103547.

[3] H.-P. Wieser *et al.*, "Development of the open-source dose calculation and optimization toolkit matrad," *Med. Phys.*, vol. 44, no. 6, pp. 2556–2568, 2017.

[4] M. A. Tewell and R. Adams. "The plunc 3D treatment planning system: A dynamic alternative to commercially available systems," *Med. Dosimetry*, vol. 29, no. 2, pp. 134–138, 2004.

[5] A. Alexander, F. Deblois, G. Stroian, K. Al-Yahya, E. Heath, and J. Seuntjens, "MMCTP: A radiotherapy research environment for Monte Carlo and patient-specific treatment planning," *Phys. Med. Biol.*, vol. 52, no. 13, pp. N297–N308, Jun. 2007.

[6] M. Rodriguez, J. Sempau, and L. Brualla, "Primo: A graphical environment for the Monte Carlo simulation of Varian and Elekta linacs," *Strahlentherapie und Onkologie*, vol. 189, no. 10, pp. 881–886, 2013.

[7] Z. A. Alrowaili *et al.*, "2D mapping of the MV photon fluence and 3D dose reconstruction in real time for quality assurance during radiotherapy treatment," *J. Instrum.*, vol. 10, no. 09, pp. P09019–P09019, Sep. 2015.

[8] L. Brualla, M. Rodriguez, and A. M. Lallena, "Monte Carlo systems used for treatment planning and dose verification," *Strahlentherapie und Onkologie*, vol. 193, no. 4, pp. 243–259, 2017.

[9] D. Hoffman, B. Dyer, C. K. Nair, Y. Katuri, Y. Rong, and S. Benedict, "SU-F-T-326: Diode array transmission detector systems evaluation," *Med. Phys.*, vol. 43, pp. 3538–3538, Jun. 2016.

[10] Y. Nakaguchi, T. Ono, M. Maruyama, Y. Shimohigashi, and Y. Ka, "Validation of a method for in vivo 3D dose reconstruction in SBRT using a new transmission detector," *J. Appl. Clin. Med. Phys.*, vol. 18, pp. 69–75, Jul. 2017.

[11] B. Poppe *et al.*, "DAVID—A translucent multi-wire transmission ionization chamber for in vivo verification of IMRT and conformal irradiation techniques," *Phys. Med. Biol.*, vol. 51, pp. 1237–1248, Mar. 2006.

[12] D. Hoffman, E. Chung, C. Hess, R. Stern, and S. Benedict, "Characterization and evaluation of an integrated quality monitoring system for online quality assurance of external beam radiation therapy," *J. Appl. Clin. Med. Phys.*, vol. 18, no. 1, pp. 40–48, 2017.

[13] L. Beck, J. J. Velthuis, S. Fletcher, J. A. Haynes, and R. F. Page, "Using a TRAPS upstream transmission detector to verify multileaf collimator positions during dynamic radiotherapy delivery," *Appl. Radiat. Isotopes*, vol. 156 Feb. 2020, Art. no. 108951.

[14] W. Snoeys, "CMOS monolithic active pixel sensors for high energy physics," *Nucl. Instrum. Methods Phys. Res. A, Accelerators Spectrometers Detectors Assoc. Equip.*, vol. 765, pp. 167–171, Nov. 2014.

[15] N. Guerrini, R. Turchettaa, G. Van Hoftenb, R. Hendersonc, G. McMullanc, and A. R. Faruqic, "A high frame rate, 16 million pixels, radiation hard CMOS sensor," *J. Instrum.*, vol. 6, Mar. 2011, Art. no. C03003.

[16] R. F. Page *et al.*, "Towards using a monolithic active pixel sensor for in vivo beam monitoring of intensity modulated radiotherapy," *Nucl. Instrum. Methods Phys. Res. A, Accelerators Spectrometers Detectors Assoc. Equip.*, vol. 731, pp. 295–298, Dec. 2013.

[17] "International patent pending," Patent pct/gb2018 050 583, Mar. 2018.

[18] F. Seif and M. R. Bayatiani, "Evaluation of electron contamination in cancer treatment with megavoltage photon beams: Monte carlo study," *J. Biomed. Phys. Eng.*, vol. 5, no. 1, pp. 31–38, Mar. 2015.

[19] S. Jan *et al.*, "GATE: A simulation toolkit for PET and SPECT," *Phys. Med. Biol.*, vol. 49, no. 19, pp. 4543–4561, Sep. 2004.

[20] S. Agostinelli *et al.*, "GEANT4—A simulation toolkit," *Nucl. Instrum. Methods Phys. Res. A, Accelerators Spectrometers Detectors Assoc. Equip.*, vol. 506, no. 3, pp. 250–303, 2003.

[21] *Oracle Cloud Infrastructure*. Accessed: Dec. 2019. [Online]. Available: https://docs.cloud.oracle.com/iaas/content/home.htm

[22] *Cluster in the Cloud*. Accessed: Dec. 2019. [Online]. Available: https://cluster-in-the-cloud.readthedocs.io/en/latest/

[23] R. Mohan, C. Chui, and L. Lidofsky, "Energy and angular distributions of photons from medical linear accelerators," *Med. Phys.*, vol. 12, no. 5, pp. 592–597, 1985.

[24] L. Urbán, "A model for multiple scattering in GEANT4," CERN Res.Inst., Geneva, Switzerland. Rep. CERN-OPEN-2006-077, Dec. 2006.

[25] K. Utitsarn *et al.*, "Impact of a monolithic silicon detector operating in transmission mode on clinical photon beams," *Physica Medica*, vol. 43, pp. 114–119, Nov. 2017.

[26] K. Utitsarn *et al.*, "Two-dimensional solid-state array detectors: A technique for in vivo dose verification in a variable effective area," *J. Appl. Clin. Med. Phys.*, vol. 20, no. 11, pp. 88–94, Nov. 2019.

[27] B. Allgaier, E. Schüle, and J. Würfel, "Dose reconstruction in the OCTAVIUS 4D phantom and in the patient without using dose information from the TPS," document D913.200.06/00, PTW Freiburg GmbH, Freiburg im Breisgau, Germany, Oct. 2013.